



Identification of the mechanical properties and surface morphology of the friction stir welding on aluminum alloy specimens

Nabil Chakroune¹ · Tahar Nateche^{1,2} · Mouna Amara² · Habib Boudaa¹ · Ibrahim Ayad¹ · Souad Makhfi³ · Rami Khalid Suleiman⁴ · Sidammar Lamsafda⁵ · Abdelmoumen Guedri⁶ · Mohammed Hadj Meliani^{2,7} · Guy Pluvinage⁷

Received: 19 September 2023 / Accepted: 5 December 2023 / Published online: 16 December 2023
© The Author(s), under exclusive licence to Springer-Verlag London Ltd., part of Springer Nature 2023

Abstract

The fracture behavior of lap-shear joints manufactured by the friction stir welding (FSW) technique is examined in this paper. Two aluminum sheets, 6 mm and 10 mm in thickness, were welded using different process parameters to form a lap-shear joint. A special tool was designed and fabricated for the stir-spot welding process. The microhardness of the joint's surface was analyzed with regard to the evolution of different parameters: the thickness and rotating speed of the tool. Static tensile tests were performed to determine the behavior of the welded joint using the two sheets. The three-point bending (TPB) and fatigue parameters of the weld were determined to characterize the fracture behavior. The effect of different main process-controlling parameters, such as the tool probe pin rotating speed, duration of action time, and sinking/penetration depth into the lower welded sheet on the weld's fracture behavior, has been investigated through an intensive experimental program. Optical and scanning electron microscope fractographs were obtained to examine the weld fracture modes in different situation. The results show that higher frictional heat due to a relatively higher tool probe pin rotational speed and penetration depth into the lower sheet produces improved joint static strength and toughness.

Keywords FSW · Aluminum · SEM observations · Toughness · Fracture behavior

✉ Mohammed Hadj Meliani
m.hadjmeliani@univ-chlef.dz

¹ Mechanical Engineering Department, Faculty of Mechanics, Oran, Algeria

² LPTPM, HassibaBenbouali University of Chlef, Hay Salem 02000, B.O.Box. 151, Chlef, Algeria

³ Department of Mechanics, Faculty of Technology, University of Ibn Khaldoun of Tiaret, BO. Box 12. 14000, Tiaret, Algeria

⁴ Interdisciplinary Research Center for Advanced Materials, KFUPM, 31261 Dhahran, Saudi Arabia

⁵ Laboratory of Materials and Energy, University of Tamanghasset, Tamanrasset airport road – 11000, B.P 10034 Tamanghasset, Algeria

⁶ Infra-Res Laboratory, Department of Mechanical Engineering, University of Souk Ahras, Souk Ahras, Algeria

⁷ L3EM-ENIM, Île de Saulcy 57045, University Paul Verlaine of Metz, Metz, France

1 Introduction

The first step of friction stir welding (FSW) was invented in 1991 at the Welding Institute in the UK [1]. The principal function is to create friction with stationary parts using a rotating and non-consumable tool that spins, moving along the joint between two components to produce high-quality butt or lap welds. This newly proposed technique has exponential applications in aerospace and rail car manufacturing, as well as with hard metals. After being primarily used to weld aluminum and a few other alloys [3, 4], friction welding has been employed to connect various types of related, similar, and dissimilar materials, including metals and non-metals [5–20]. Regarding experimental results [21–24], FSW can be used on materials with different geometric forms [25–30], especially those with thicknesses below 1 mm, as well as on workpieces up to 75-mm thick. The low-density alloy combines weight reduction with lower assembly and maintenance costs, and when combined with advanced welding practices

and aerostructure redesign, it offers up to 25% weight reduction [31]. Various types of combined loading, such as tension, compression, flexion, and fatigue, are essential parameters that should be considered in the design of structures, especially when they are welded using FSW. Several factors influence the quality and properties of the weld using the new FSW process, depending on (i) the machine and the tool used, (ii) the specimen, and (iii) the mode of fixation and connection. Most of these factors are related to pressure and friction time, pressure and forging time, rotational speed, oscillation frequency, oscillation amplitude, friction pressure, and their correlation with microstructure characterization, microhardness fluctuation, interfacial phase formation, optimal welding parameters, and mechanical properties [32–35]. Useful studies have characterized the mechanical properties of FSW aluminum alloys under static tensile loading [36, 37] and fatigue conditions [38–40], both before and after welding. Generally, 90% of failures in aluminum structures are initiated by fatigue phenomena. The FSW method improved fatigue performance by approximately 2.4 times compared to the single riveting method, ensuring mechanical properties and in-service fatigue life [41, 42]. The authors in [43] investigated the mechanical properties and residual stresses of FSW aluminum 5083 for tensile test specimens. The results confirm the sensitivity of the joint surface to thermal input rather than the mechanical deformation caused by the FSW tool. In [44, 45], it showed that static tensile shear strength increased with decreasing tool rotational speed and increasing tool holding time, while cross tension strength decreased with increasing both parameters. The results of microstructure confirmed the presence of two fracture modes: nugget shear fracture mode and mixed mode under tensile shear loading. Experimental studies [44–56] on friction stir spot welding for several types of aluminum have shown that rotational speed has a significant effect on the mechanical effectiveness of the joint weld. Akinlabi et al. [48] investigated tensile strength using different welding parameters such as tool size and rotational and traverse speed on Al/Cu specimens using SWP. The joint efficiency was 86% with a rotational speed of 950 tr/min and a feed rate of 50 mm/min using an 18-mm shoulder diameter tool. Nandan et al. [49] studied technical properties and residual constraints based on welding speed, showing that using a constant material property affects the model's accuracy within the temperature domain. Riahi et al. [50] analyzed transient temperature and thermal constraints, where heat is generated due to friction between the tool and the workpiece, and the thermal behavior of the welded piece was considered an input heat for an elastoplastic model predicting residual stress. Additionally, heat distribution across the thickness varied and appeared asymmetrical. Veljić et al. [51] investigated heat generation during the plunge phase in FSW, where the influence of heat generated by friction surpassed plastic deformation. The sliding rate of the tool and the temperature

relative to the workpiece are linked to heat generated by friction, and the material's speed is linked to heat generated by plastic deformation. Al-Badour et al. [52] conducted investigations using FEM for FSW, taking into account adiabatic heating effect and estimating the maximum temperature equal to the material's solidus temperature (583 °C) defined in the Johnson–Cook material model. Bussetta et al. [53] modeled the thermomechanical behavior of FSW, with both fluid and different solid formulas yielding the same results. Aziz et al. [54] studied the effect of rotational speed on heat generation, proving it to be more significant than the traverse speed. Sun et al. [55] predicted temperature peaks and residual stresses, demonstrating that the Fixed Shoulder FSW (SSFSW) process produced a narrower and more uniform weld nugget and heat-affected zone compared to conventional FSW. Garg and Bhattacharya [56] studied the influence of different tool pin shapes, tool rotation speed, and dwell time on shear strength around FSW, with the tool rotation speed and pin shape significantly influencing shear strength. Jain et al. [57] (studied temperature and stress distribution, predicting the temperature distribution on the workpiece and tool, with the maximum temperature observed higher on the upper surface of the piece. Maisonneuve et al. [58] analyzed transient temperature and thermal stresses, often proposing assumptions and simplifications for FSW simulation, resulting in good agreement. The temperature continuously varied, initially increasing during heating and then decreasing during cooling without a pause at the highest temperature point (Palanivel et al. [59]). While valuable studies focusing on fatigue and microstructural issues in FSW aluminum structures have been undertaken, there is still a lack of studies on the characterization of material properties for FSW high-strength aluminum alloys, such as aluminum 2017AA, used for shipbuilding. Although several studies have addressed microstructural and fatigue aspects in FSW aluminum structures, there remains a dearth of research pertaining to the characterization of material properties specifically for high-strength aluminum alloys used in shipbuilding, such as aluminum 7000 and 7070.

The sampling direction in friction stir welding of aluminum alloys holds significant importance, alongside other crucial factors, for maximizing its application. Specimens can be sampled either perpendicular or longitudinal to the weld direction. Cutting the specimens longitudinally (parallel to the direction of the joint), FSW of aluminum alloys provides valuable information about the weld characteristics, aids in understanding the welding process, facilitates mechanical property evaluation, and contributes to process optimization in aluminum alloys. However, it is important to note that the specific novelty and significance of this approach may vary depending on the context and the research study or development being referred to.

The primary aim of this study is to offer a comprehensive analysis of the mechanical properties exhibited by friction

stir welded aluminum alloys. Four crucial analyses have been conducted to assess the strength and durability of the welding joint. The findings and conclusions derived from this study are meticulously documented, along with a comprehensive description of the test database.

1.1 Method of analysis and experimental tests

In this section, the various experimental methods are described. Initially, the conducted mechanical tests and the procedures employed to determine mechanical behaviors under conditions such as tensile, flexural, and fatigue loading are presented.

1.1.1 Chemical composition and microstructural observations

In this study, a base material investigated is an alloy from the 2000 series (aluminum-copper). The alloy used for conducting welds exhibits a structural hardening known as “Age-hardening” with a designation of AU4G-1). The alloy was examined in a metallurgical condition known as T6, which corresponds to the as-received state of the sheet. Chemical analyses were conducted using X-ray fluorescence spectrometry. The chemical composition of the 2017AA alloy is provided in Table 1.

Plates measuring 100 mm in width and 250 mm in length were cut from a 6 mm and 10-mm thick 2017AA metal sheet using an industrial saw. All welding tools were manufactured from H11 steel (tool steel Z38CDV5.1), which has a higher melting temperature and hardness compared to aluminum. Table 2 presents the chemical composition of this steel.

Observations were conducted using an optical microscope of the brand “Leica DM 2500 M,” connected to a microcomputer equipped with “Leica Application Suite LAS” image acquisition software, which facilitates the transfer and processing of these images. To characterize the microstructure of the welded joints and identify different zones, a Keller reagent etching was performed. Prior to etching, the sample must be mechanically polished using 240-grade paper to achieve a mirror finish, followed by polishing with 3 μ m diamond paste. The metallographic etching involves immersing the sample in the Keller reagent (2.5 ml nitric acid HNO₃, 1 ml hydrofluoric acid HF, 1.5 ml hydrochloric acid HCl, and 95

ml distilled water) for 10 s, followed by rinsing with distilled water. Micrographic examinations of the sample surfaces are conducted using a scanning electron microscope of the QUANTA 600FEI type, equipped with an infrared camera.

1.1.2 Mechanical characterization methods

Microhardness measurements HV0.5 were performed using an “HWDM-1” instrument connected to a computer equipped with “C.A.M.S” measurement and image acquisition software. The determination of microhardness values will be conducted based on these images. Measurements were carried out following the NF EN ISO 6507–1 standard with a 500-g load applied for 15 s. The spacing between two measurement points is 1 mm. Profiles taken at 1/4 thickness, midpoint, and 3/4 thickness positions in the 2017AA alloy allowed us to verify that the hardness values were of similar magnitude across the sheet thickness. As previously discussed, a Friction Stir Welding (FSW) joint consists of distinct microstructural zones, each with different characteristics. The mechanical properties of each zone are directly linked to their microstructure. Extracting micro-specimens to determine the mechanical properties of each joint zone is relatively challenging. Therefore, we analyze the overall behavior of the weld beads. Subsequently, we will analyze fracture surfaces to correlate this information with microstructural parameters. A comparative study of obtained weld joints was conducted, considering various parameters with the base material. This is essential for establishing a connection between mechanical performance results and process operational parameters. Tensile testing was conducted following the ASTM E08 standard to assess the mechanical properties of both the base material and FSW weld joints, particularly the static behavior law (stress–strain curve). Tensile tests were performed on specimens using a Zwick/Roell ZMART.PRO type universal testing machine with a maximum capacity of 200 kN. The tests were conducted at a crosshead speed of 4 mm/min. Test control and data acquisition were facilitated by the Test Xpert II software. Bending tests were carried out in accordance with the NF A 89–204 standard on carefully machined welded and non-welded specimens. Fatigue tests were performed under plane bending with a load ratio $R = -1$, at a frequency of 25 Hz.

Table 1 Chemical composition of the base metal (2017AA) determined by X-ray

Elements	Si	Fe	Cu	Mn	Mg	Zn	Ti	Cr	Al
%Weight	0.38	0.52	1.36	0.27	2.23	5.74	0.19	0.22	89.09

Table 2 Chemical composition of tool steel Z38CDV5.1

Elements	C	Si	V	Cr	Mn	Fe	Ni	Cu	Mo
%Weight	0.393	0.110	0.293	4.567	0.926	92.054	0.165	0.076	1.016

The objectives of these tests were, firstly, to compare the cycles to failure of different tested welds and, secondly, to study weld damage using non-linear acoustic techniques.

2 Results of mechanical tests on welds

2.1 Microhardness mapping

2.1.1 Microhardness mapping on 6 mm and 10 mm samples of thickness

To examine hardness variation across a cross-section of an FSW (friction stir welding) bead, a microhardness mapping was conducted. Measurements were taken at different depths from the bead surface (1.5 mm, 3 mm, and 4.5 mm).

Figure 1 illustrates the microhardness curves for three FSW weld beads. The welds were created at a welding speed of 0.6 mm/s and three rotational speeds: 950 rpm (Fig. 1a), 1050 rpm (Fig. 1b), and 1250 rpm (Fig. 1c). The tests were repeated 5 to 7 times, depending on the availability of the test pieces with error values in a range of 8–12%. Figure 1 demonstrates the classic “W” shape where hardness is minimal in the HAZ (heat affected zone), the area that experienced over-aging. It also indicates that the minimum hardness value is nearly the same on both sides of the joint (AS and RS). The three measurement lines correspond to those presented in Fig. 1; the numbering of the lines starts from the closest to the upper surface of the joint (line 1/4 thickness). Hardness in the weld nugget is lower than the base metal but higher than that of the HAZ. This characteristic is typical for FSW joints in structurally hardened aluminum

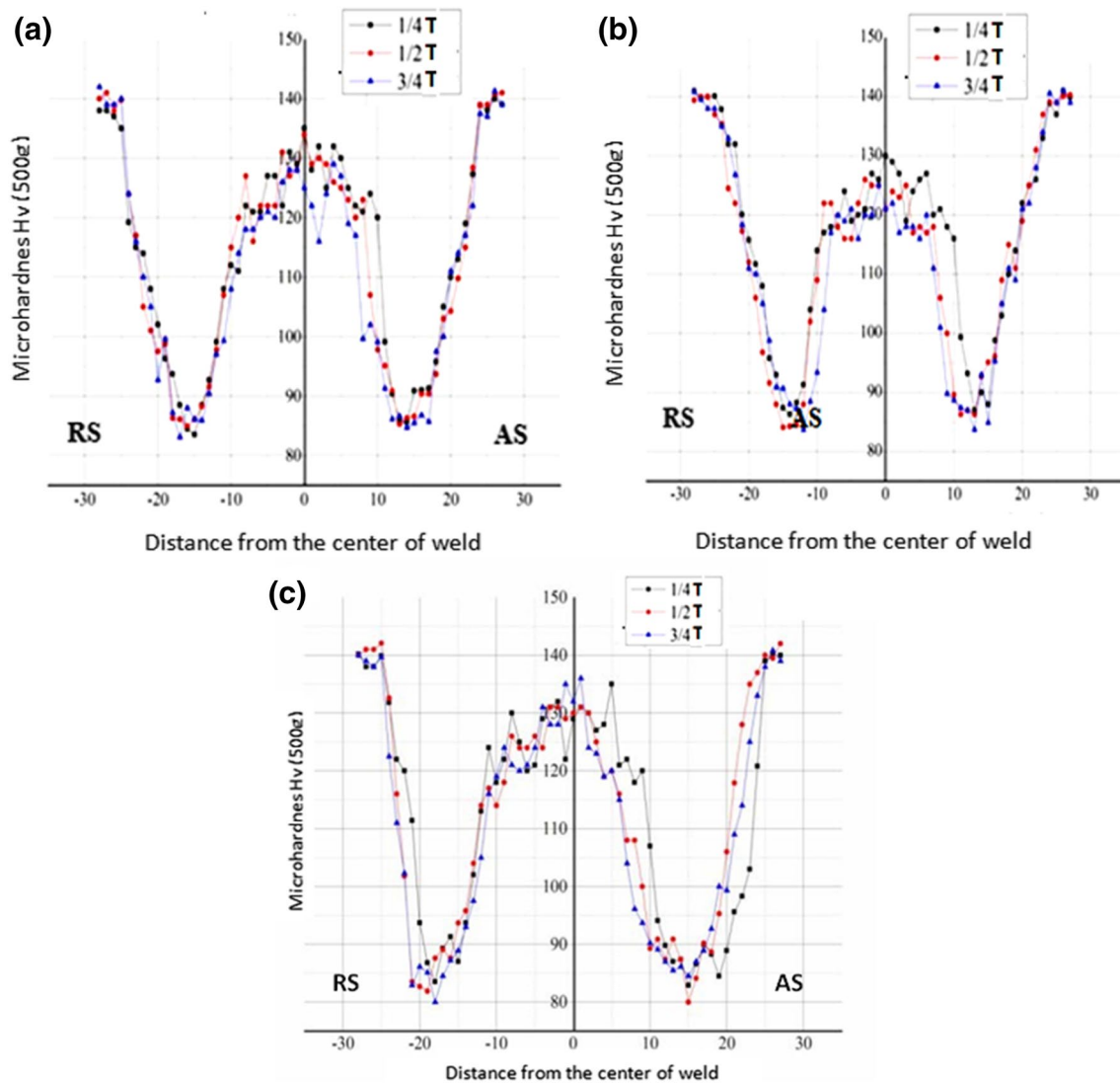


Fig. 1 Illustration of the microhardness curves for three FSW weld beads: a 950 rpm, b 1050 rpm, and c 1250 rpm

alloys. The microhardness map reveals that hardness does not vary across the thickness; the values measured on the three lines are very close. Welding causes softening and thus a decrease in hardness across the weld. This drop in hardness occurs within the HAZ, where values shift from 140 to 85 Hv over just a few millimeters. The thermo-mechanically affected zone (TMAZ) shows a minimum hardness, while within the weld nugget, it rises to an average value of 130 Hv. The hardness curve allows deducing the extent of the different zones; the dimensions of the various zones in the welded joint are summarized in Table 3. Welding 10-mm-thick plates presents a similar hardness profile to the 6-mm joint (Fig. 2). It is worth noting that hardness also varies across the thickness of the welded joints, with maximum values at the 1/4 thickness line of the sample. The values measured at half and 3/4 thickness (noted by T) are the lowest among the measurement lines. It can be observed that microhardness decreases slightly less in the depth of the welds at 1250 rpm compared to the welds at 1450 rpm. Figure 2b displays a decrease of about 25 HV between the top and bottom of the weld for the joints at 1450 rpm. The dimensions of the different zones in the welded joint are summarized in Table 3.

Table 3 Summary of the approximate size of the zones in a joint welded by FSW on alloy 2017AA of 6-mm thick

Zones	ZAT/RS	ZATM/RS	Noyau	ZATM/AS	ZAT/AS
Dimension (mm)	8–10	4–5	18–20	6–7	1–4
Dimension (mm)	8–10	6–7	15–17	3–4	1–4

2.1.2 Effect of rotation speed

To investigate the impact of rotation speed, measurements are taken along the midline of the sample (1/2 of the thickness), and microhardness curves are plotted for various speeds. The comparison of the microhardness profiles of the three weld beads, produced at rotation speeds of 950, 1050, and 1250 RPM, reveals that the rotational speed has no influence on the hardness in the 6-mm-thick samples (Fig. 3.a).

Along the weld plates produced by FSW, starting from the base material's microhardness value of 140 HV, the microhardness profile drops rapidly within the heat affected zone (HAZ) until reaching a minimum value of 85 HV within the HAZ close to the near-side HAZ at – 15 mm from the center of the joint (RS side) and at 12 mm from the center of the joint (AS side). The microhardness then increases within the thermo-mechanically affected zone (TMAZ), reaching a stable value of 130 HV in the nugget, which is close to that of the base material. For the 10-mm-thick samples, it can be observed that the microhardness trend obtained at a rotation speed of 1450 rpm is slightly higher than that obtained at a speed of 1250 rpm (Fig. 3b). In this case, the rotation speed indeed influences the microhardness of the 10-mm-thick joints.

2.1.3 Tensile tests

Several test specimens containing welds produced at different rotation speeds were subjected to tensile tests. These mechanical tests aimed to characterize the welds and define a range of speeds that would yield maximum tensile strength for plates of 6 and 10-mm thickness. The tests were conducted at room temperature. Table 4 presents the mechanical properties obtained from three trials.

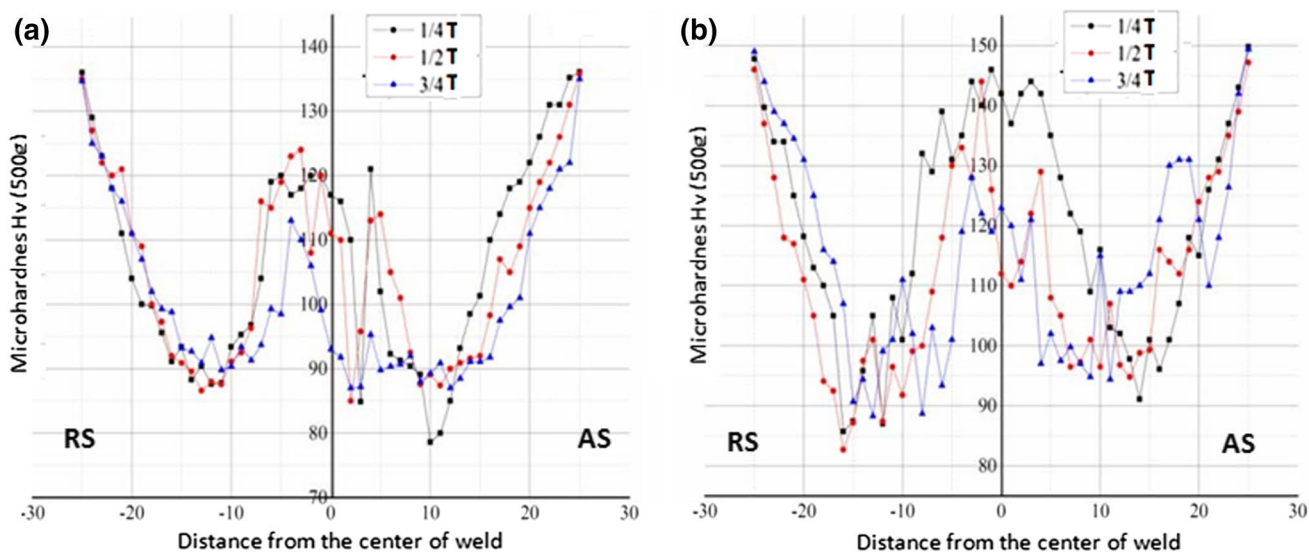


Fig. 2 Mapping of microhardness HV500g of the seal 10-mm thickness 2017AA alloy welded at rpm: **a** 1250 rpm and **b** 1450 rpm

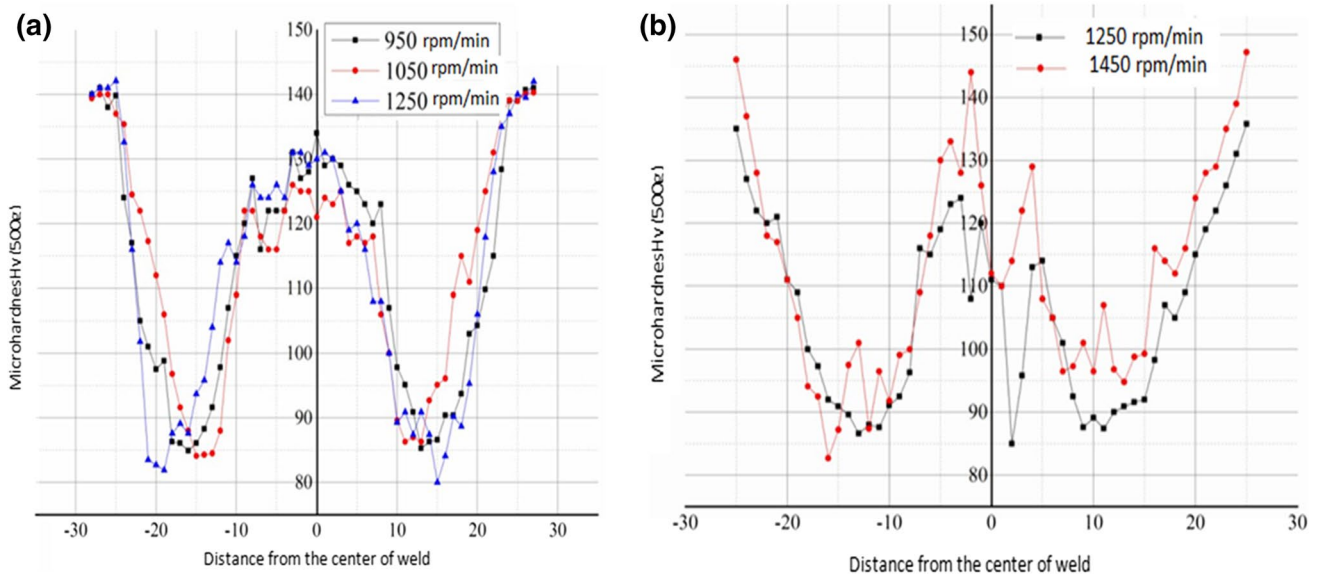


Fig. 3 HV500g microhardness mapping of welded joint: **a** 6-mm thickness alloy 2017AA at different tool rotation speeds and **b** 10 mm

From the tensile tests conducted on the specimens outlined in Table 4, several observations can be drawn. According to these results, the values obtained after welding are consistently lower than those of the base material, whether in terms of yield strength, ultimate strength, or elongation at rupture. The welded joints at 950 and 1250 RPM exhibit the highest tensile strength and good ductility, while the joint

welded at 1050 RPM maintains good tensile strength but undergoes a significant loss of ductility. The reduction in yield strength and tensile strength is primarily attributed to the decrease in joint hardness. As an example, Fig. 4 presents the stress–strain curves for the base metal and welded specimens of the 2017AA alloy, highlighting the three distinct phases of a stress–strain curve.

Table 4 Mechanical properties obtained by the tensile test on weld joints

Specimen	Conditions	Yield strength R_e [MPa]		Tensile strength R_m [MPa]		Elongation at fracture A [%]	
		Values	average	Values	Average	Values	Average
6 mm	BM	463	470	504	500	22.5	21.87
		450		490		21.7	
		497		510		21.2	
	950 tr/min	259	257.5	353.6	351.03	12.24	12.18
		257.5		351		12.19	
		256		348.5		12.12	
	1050 tr/min	270	268.67	316	315.83	9.5	9.5
		277		319.5		9.2	
		259		312		9.8	
1250 tr/min	232	238	337	340.67	13.9	14.07	
	239		343		14.2		
	243		342		14.1		
10 mm	1250 tr/min	134	137.67	141	145.17	8.35	8.48
		135		145		8.5	
		144		149.5		8.6	
	1450 tr/min	220	217	225	219.67	12.6	12.27
		214		219		12	
		217		215		12.2	

Globally, it is generally observed that the rotational speed has little influence on the yield strength and tensile strength. As evident from Fig. 4, it is clear that better mechanical quality is achieved with a rotation speed of 1250 rpm. Additionally, it can be observed that the plastic zone is relatively narrow for the welded specimens, indicating a predominantly brittle fracture behavior. The fracture of the 6-mm-thick samples occurred at the center

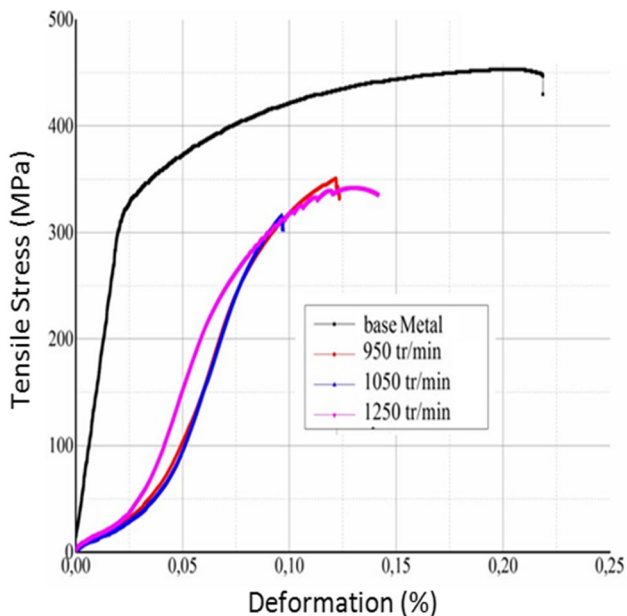
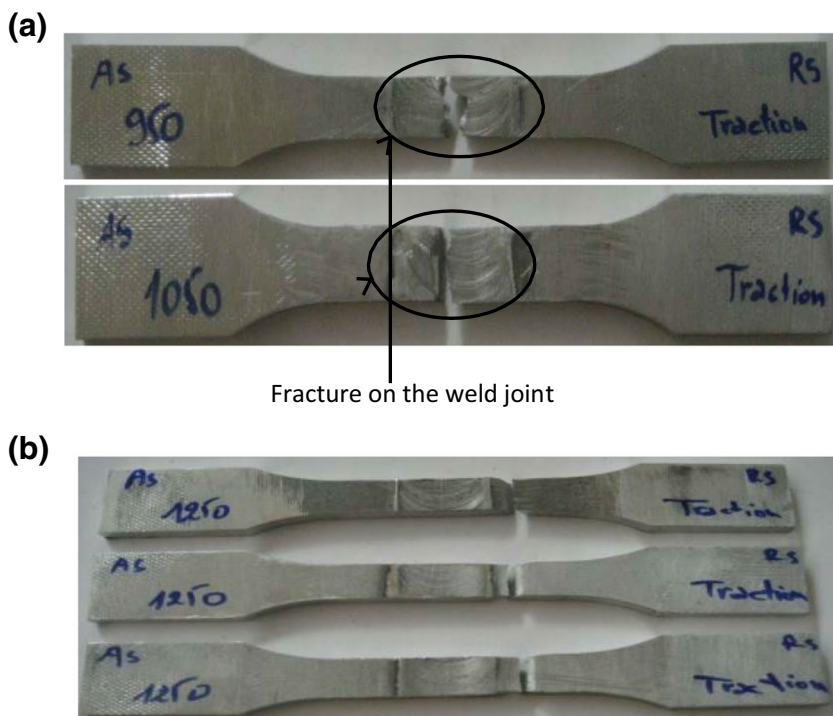


Fig. 4 Stress–strain curves for 6-mm-thick specimens

Fig. 5 **a** Fracture within the joint for both 6-mm-thick samples and **b** fracture outside the welds at 1250 rpm



of the joint (Fig. 5a) for welds at 950 and 1050 rpm. For joints welded at 1250 rpm, the fracture is situated within the heat-affected zone on the recoil side (RS) (Fig. 5b). Notably, fractures are observed at the edge of the bead within the heat-affected zone, which exhibits lower hardness due to material softening. Regarding the welds on 10-mm plates, a significant decrease in mechanical properties is noticeable, encompassing both yield strength and maximum tensile strength. The loss of ductility in these joints is also substantial. These reductions can be attributed to the presence of defects within the joints, leading to diminished joint quality. Figure 6 provides an illustrative example of the stress–strain curves for the base metal and the welded specimens.

Regarding the 10-mm-thick plates, the fracture occurs within the weld joint, whether it is for welds produced at 1250 rpm or at 1450 rpm. Despite the fact that FSW-welded assemblies still exhibit acceptable mechanical properties, it is worthwhile to determine the efficiency coefficient of the weld joints (Fig. 7).

2.1.4 Weld joint efficiency coefficient for FSW

The weld joint efficiency coefficient is defined as the ratio of the tensile strength of the welded assembly to the tensile strength of the base metal. The efficiency coefficient of the joints is obviously dependent on both the welding parameters and the material. The calculation results are presented in Table 5. The following are the obtained weld joint efficiency coefficients:

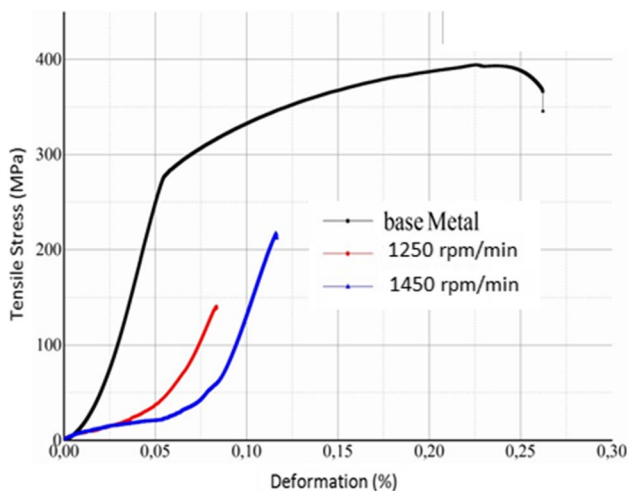


Fig. 6 Stress–strain curves for 10-mm-thick specimens

Joint Efficiency Coefficient = $(R_m \text{ Tensile Strength of Welded Joint}) / (R_m \text{ Tensile Strength of Base Metal})$.

First and foremost, the weld with the highest ultimate tensile strength (measuring 351.03 MPa) was performed at a rotation speed of 950 rpm. Its efficiency is evaluated at approximately 70.2% of the base material’s tensile strength, which is established at 500 MPa. When comparing this weld to those performed at rotation speeds of 1250 and 1050 rpm, its efficiency is relatively low. Similarly, considering the welds performed on 10-mm plates, the one executed at a rotation speed of 1450 rpm exhibits high efficiency. In conclusion, the tensile tests reveal that the best welds, with a maximum rupture strength (R_m) exceeding 315 MPa ($R_m > 315$), were achieved on 6-mm-thick plates regardless of the rotation speed used. In contrast, the welds performed on 10-mm plates exhibit the most degraded properties.

2.1.5 Fracture facies analysis

Microscopic observations were conducted on the fracture facies of each ruptured specimen. For all 6-mm-thick specimens welded at 1250 rpm, the fracture consistently occurs on the side opposite the welding direction at the boundary

Fig. 7 Fracture in the weld joint for 10-mm thickness specimens

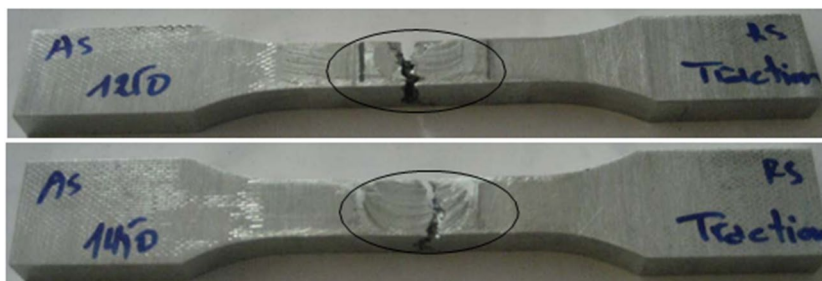


Table 5 Weld joint efficiency coefficients for different welds

Plates	Rotational speed N (tr/min)	Coefficient of efficiency (%)	Lieu de rupture
6 mm	950	70.2	In the joint
	1050	63.16	In the joint
	1250	68.13	edge of the ZAT cord on the RS side
10 mm	1250	29.03	In the joint
	1450	43.93	In the joint

between the thermo-mechanically affected zone and the thermally affected zone of the weld joint. The obtained fracture facies are oriented at a 45° angle relative to the specimen surfaces. Visualization of the fracture facies was carried out using a scanning electron microscope (SEM). Figure 8 presents an SEM image taken perpendicular to the axis of the tensile specimen.

In Fig. 8, the ductile nature of the fracture is evident. Additionally, the fracture facies reveal the presence of multiple dimples. These dimples elongate in the direction of tension, aggregate, and coalesce to expedite the fracture process. Figure 9 illustrates the observation using a scanning electron microscope of the fracture facies in a weld joint produced by FSW at a speed of 950 rpm. Cavities are noticeable in areas rich in precipitates, indicating a ductile mode of fracture in this case.

However, for the welded joints at 1050 rpm, the analyses make it possible to distinguish mainly two areas: a ductile rupture zone where SEM observations reveal the presence of cupules (Zone 1, Fig. 10) and another area of sudden rupture. The presence of cavities is noted in precipitate-rich areas across the ductile rupture zone. In the sudden rupture, a smooth area (Zone 2) is observed in comparison to the ductile rupture zone (Zone 1).

2.2 Three-point bending test

All conducted tests are stopped as soon as the punch is no longer applied along the axis of the FSW weld. The results obtained during each test (maximum force, corresponding

Fig. 8 SEM observation (various magnifications) of a tensile fracture surface of the FSW-welded joint in 2017AA alloy at a rotation speed of 1250 rpm

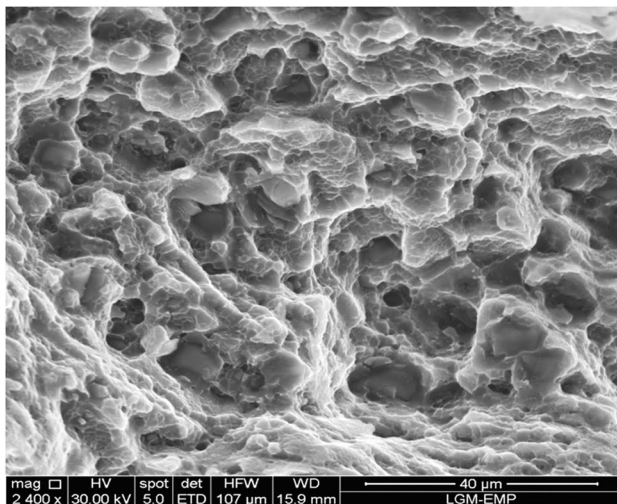
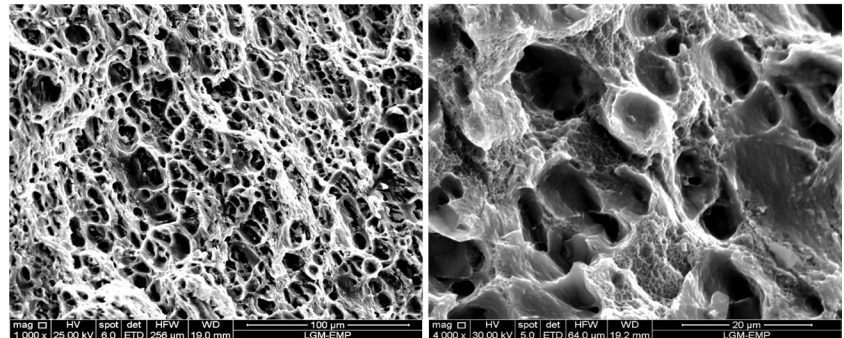
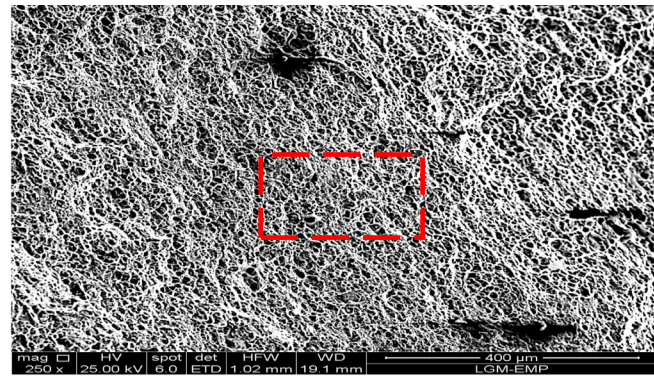


Fig. 9 Fracture morphology of a welded specimen by FSW

displacement at maximum force, and the angle after bending the Φ specimen) are recorded in Table 6 for both the 6 mm and 10-mm thicknesses. For the 6-mm thicknesses, an example of the samples after the three-point bending tests is shown in Fig. 10. After subjecting the samples to the three-point bending test, a visual inspection was carried out, revealing no cracks or tears on the 6-mm weld bead for the base metal and the specimens welded at 950 rpm. These results demonstrate excellent ductility of the specimens (Figs. 10a and 11). However, fractures in the weld

joints are observable on the specimens welded at 1050 and 1250 rpm after bending. These results indicate that specimens with superior tensile mechanical characteristics, such as those welded at 1250 rpm, do not necessarily yield the same results in three-point bending (Fig. 10b,c). Samples after the three-point bending tests are presented in Fig. 11 for the 10-mm thickness. After subjecting the samples to the three-point bending test, a visual inspection was performed, revealing no cracks or tears on the 6-mm weld bead for the base metal and the specimens welded at 950 RPM. These results once again confirm the high ductility of the specimens (Fig. 11a). However, fractures in the weld joints are observable on the specimens welded at 1050 and 1250 rpm after bending. These results indicate that specimens with superior tensile mechanical characteristics, such as those welded at 1250 rpm, do not necessarily yield the same results in three-point bending (Fig. 11b,c).

Regarding the 10-mm thickness, the absence of the plastic range was observed for the welded specimens. This is attributed to the brittleness of the joints and the presence of internal defects such as lack of penetration. For all the specimens subjected to three-point bending tests, fracture occurred at the midpoint of the joint. Fig. 12

2.2.1 Fatigue tests in plane bending

In order to demonstrate the fatigue resistance difference between a friction stir welded (FSW) joint and its associated base material, a comparison was conducted on

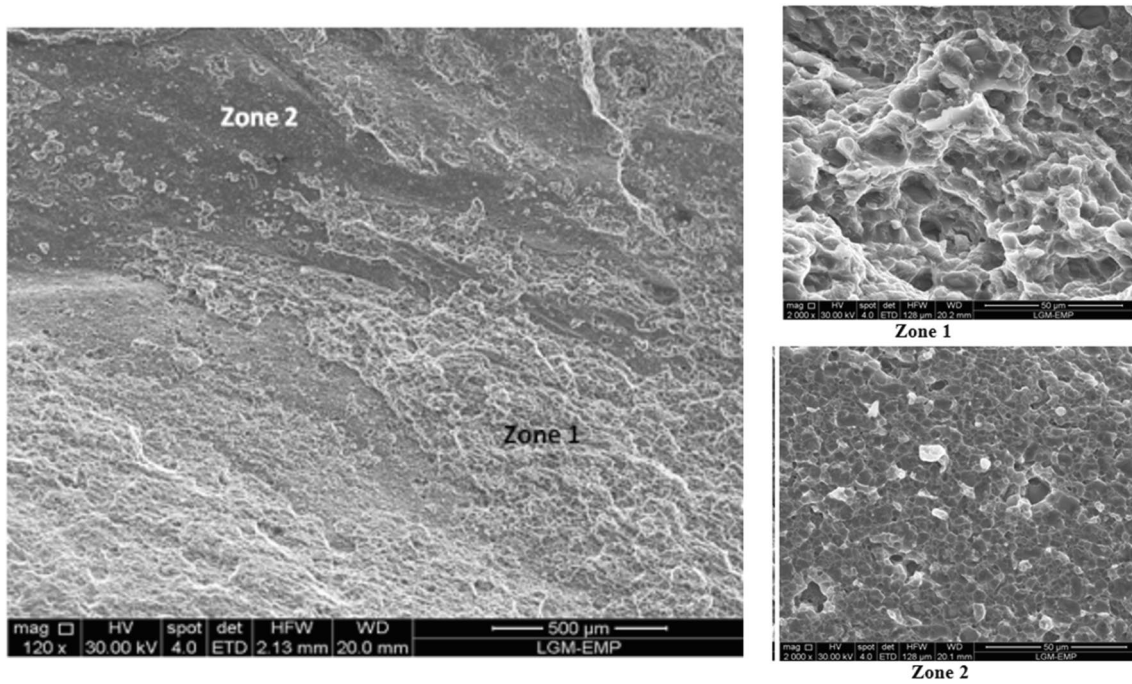


Fig. 10 Fracture surface of a weld specimen produced by FSW and tested under tension

Table 6 Mechanical properties obtained through the three-point bending test on weld joints

Specimen	Condition	Fmax (N)		Displacement (mm)		The angle Φ after folding
		Values	Average	Values	Average	
6 mm	Base metal	2395	2392.08	20.16	19.75	$\Phi \approx 139^\circ$
		2389.15		19.34		
	950	1598.79	1607.40	19.25	20.19	$\Phi \approx 137.5^\circ$
		1616		21.13		
	1050	1796.34	1799.05	20.45	21.28	$\Phi \approx 137.75^\circ$
		1801.75		22.11		
1250	1467.55	1467.79	10.49	10.50	$\Phi \approx 155.5^\circ$	
	1468.03		10.52			
10 mm	Base metal	2549.58	2548.06	11.30	11.16	$\Phi \approx 129.5^\circ$
		2546.53		11.07		
	1250	1350	1324.50	1.29	1.27	$\Phi \approx 165.75^\circ$
		1299		1.25		
	1450	2202	2189.88	2.69	2.55	$\Phi \approx 177.5^\circ$
		2177.76		2.40		

Fig. 11 Three-point bending tests of the base metal and 6-mm welded samples at rotation speeds of **a** 950 rpm, **b** 1250 rpm, and **c** 1050 rpm

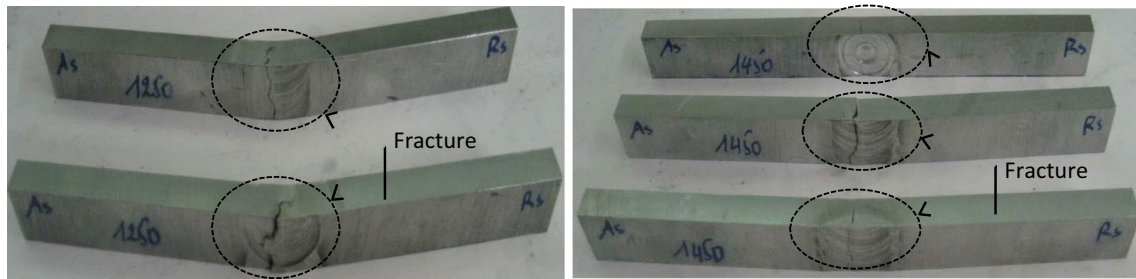
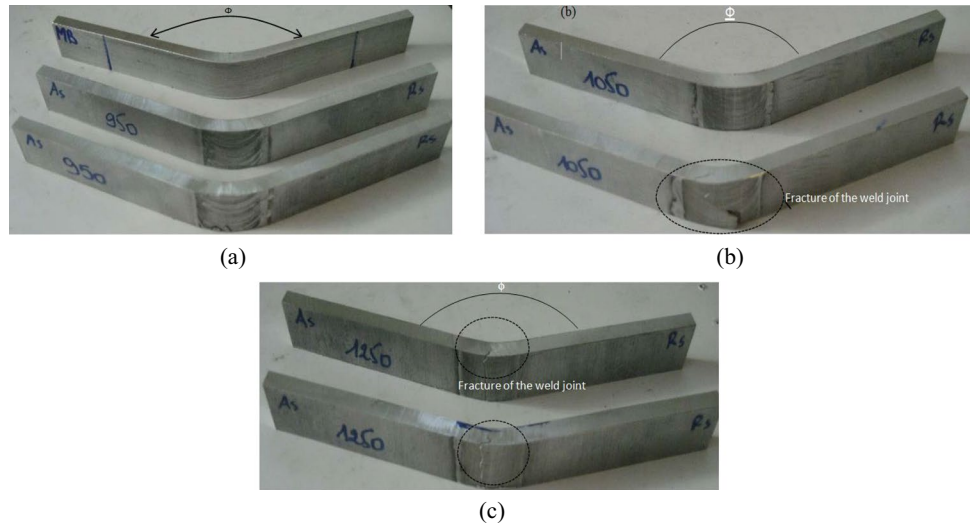


Fig. 12 Three-point bending tests of 10-mm samples welded at rotation speeds of 1250 rpm and 1450 rpm

several welds made from aerospace structural hardening alloys, specifically using the 2017AA alloy. Specimens with 6 mm and 10-mm FSW welds were tested in the as-welded condition using plane bending fatigue tests. Test conditions are provided in Section II.2. The results of the plane bending fatigue tests are presented in Table 7.

Figures 13a and b provide a comparison of the number of cycles to failure for the base metal and different FSW (friction stir welding) welds for the two thicknesses.

Based on the fatigue results, it was observed that the 6-mm-thick joint welded at a rotation speed of 1250 rpm has the best service life (1.47×10^5 cycles), with a decrease of approximately 21% compared to the base metal’s lifespan (1.87×10^5). The other two specimens welded at 950 and 1050 rpm respectively show service lives of 1.09×10^5 and 1.13×10^5 cycles. It was also noted that as the tool rotation speed increases, the service life of the obtained joint improves. The reduction in fatigue strength of the FSW (friction stir welding) joints compared to the base metal can be explained by the decrease in yield strength as observed in the

Table 7 Mechanical properties after fatigue tests in plane bending of weld joints

Test specimen	Conditions	Conditions applied constraint (MPa)	Number of cycles to failure (cycles)	
			Values	Average
6 mm	Base metal	260	180,900	1.87×10^5
	950 rpm/min		195,000	1.09×10^5
			111,800	
	1050 rpm/min		112,500	1.13×10^5
10 mm	Base metal	260	144,000	1.47×10^5
			151,300	1.64×10^5
			160,500	
10 mm	1250 rpm/min	260	24,000	2.32×10^4
			22,500	3.37×10^4
			1450 rpm/min	
			39,000	

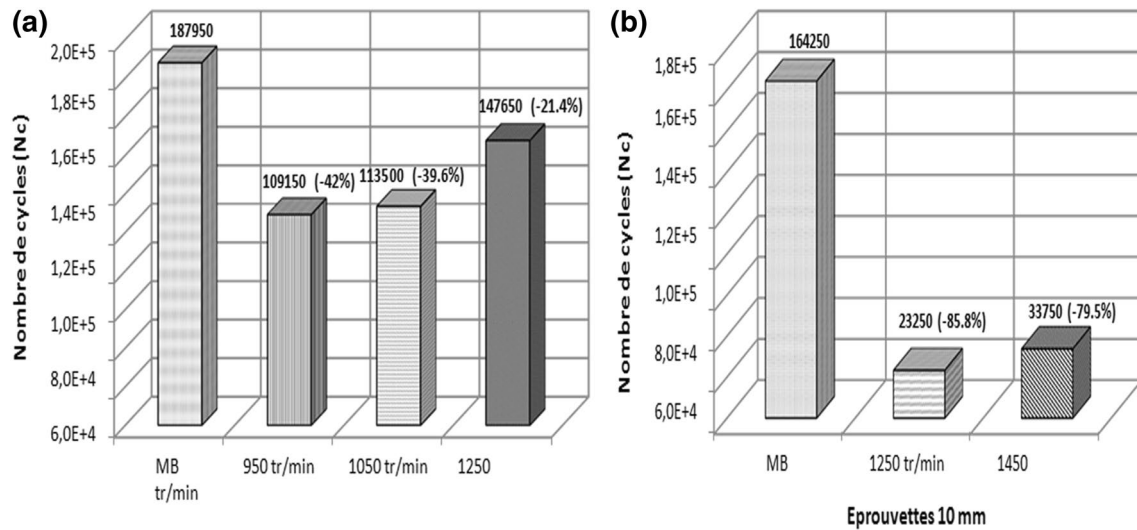
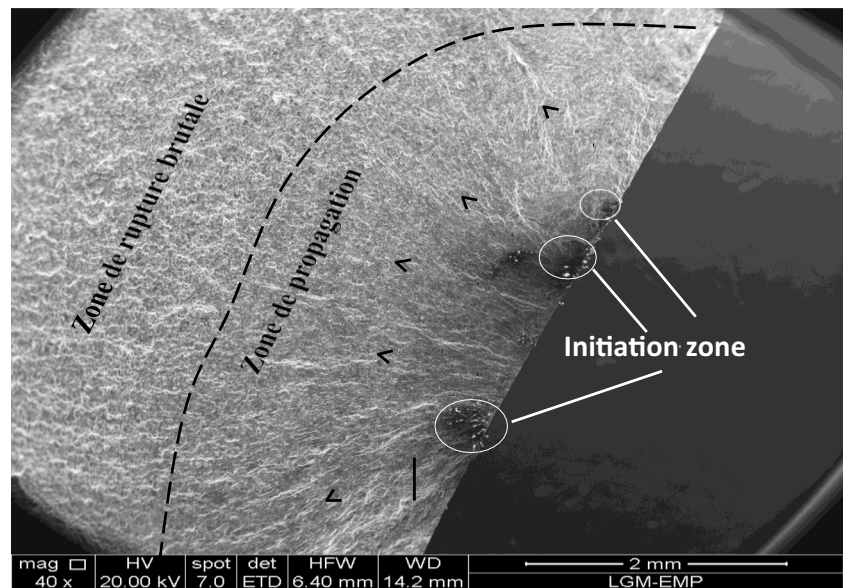


Fig. 13 Comparison of the number of cycles to failure at 260 MPa for different friction stir welding (FSW) joints with **a** 6 mm and **b** 10-mm thickness

Fig. 14 Typical appearance of the plane fatigue rupture morphology of the FSW weld joint at 1050 rpm.



tensile test. Additionally, the presence of tool groove traces is still evident even after surface treatment. For the 10-mm-thick specimens, the fatigue results confirm those obtained from the tensile and three-point bending tests. These results are very poor due to the presence of internal defects in the weld joints. In this context, we present an analysis of the fracture surfaces of the tested specimens. By focusing on

the crack initiation location, it is evident that the potential rupture zones vary for each of the welding configurations.

The fracture facies of the test specimens were observed under a scanning electron microscope (SEM) in order to identify the zones and the crack initiation mechanisms that led to the failure of the joints welded by FSW. Fig. 14 illustrates the typical appearance of the fatigue fracture surfaces

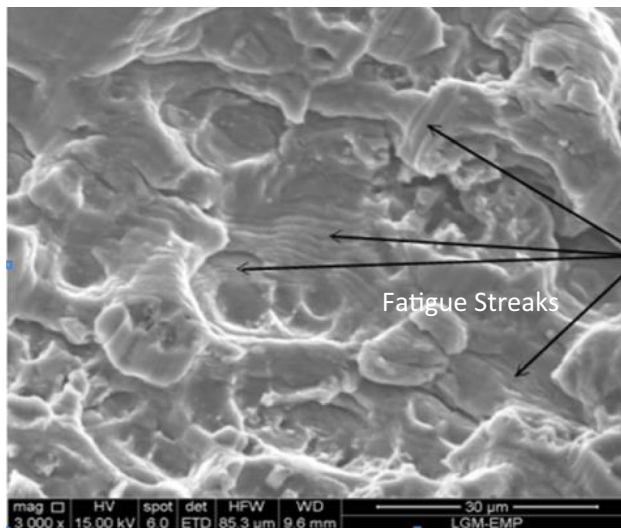


Fig. 15 SEM observation of the fatigue streaks

of the specimens. We note that there are three stages before the final rupture: crack initiation, a zone of propagation, and finally a zone of sudden rupture. Note that several initiation sites can be observed on the same fracture facies; this suggests that the fracture is associated with the coalescence of several cracks. In Fig. 15, fatigue “striations” can be seen on the fracture surfaces, which are typical of fatigue propagation.

3 Conclusion

The objective of the present study has been oriented on the collect test database on mechanical properties of friction stir welded of local aluminum alloys produce in the region. The advantages of the FSW techniques include reduced cost, improved quality, and flexibility. A series of tensile specimen’s tests, three points bending and fatigue, were undertaken on friction stir and fusion welded aluminum alloys as well as base alloys. All the tests were taken a care to analyze the microstructure and microhardness, and optical and SEM micrography have been conducted. Fractographic analysis indicated that all the joints exhibited a ductile fracture behavior when subjected to mechanical testing, further supporting the presence of favorable mechanical properties. Further study is required to obtain the optimal process parameters and tool geometry for improving the strength and fracture mechanical properties of the FSW joints of the proposal aluminum alloy. The findings highlighted the distinctive microstructural differences, variations in microhardness, ultimate tensile strength, and elongation between the FSW longitudinal and transverse joints. These insights contribute to a deeper

understanding of the joint characteristics and performance, aiding in the development and optimization of friction stir welding processes for aluminum alloy joints.

Author contribution N.C., T.N., M.A., H.B., I.A., S.M., and M.H.M. conceived and designed the experiments; R.K.S., S.L., and A.G. carried out the experiments; M.H.M., R.K.S., and G.P. analyzed the experimental data and wrote the manuscript. All authors have read and agreed to the published version of the manuscript.

Declarations

Conflict of interest The authors declare no competing interests.

References

1. Thomas WM, Temple-Smith P (TWI, rights transferred to Lead Sheet Association): 'Friction welding sheet material'. UK Patent Application GB 2 319 977 A.
2. Nasution AK, Gustami H, Suprastio S, Fadillah MA, Octavia J, Saidin S (2022) Potential use of friction welding for fabricating semi-biodegradable bone screws. *Int J Automot Mech Eng* 19:9660–9667
3. Rhodes CG, Mahoney MW, Bingel WH (1997) Effects of friction stir welding on microstructure of 7075 aluminum. *ScriptaMaterialia* 36(1):69–75
4. Hagstrom J, Sandstrom R (1998) Static and dynamic properties of joints in thin-walled aluminum extrusions, welded with different methods. *Proceedings of 6th International Conference on Aluminum Alloys*, Toyohashi, Japan, pp.1447–1452.
5. Hashimoto T, Nishikawa N, Tazaki S, Enomoto M (1998) Mechanical properties of joints for aluminum alloys with friction stir welding process. *Proceedings of 7th International Conference on Joints in Aluminum*, Cambridge, UK, 15–17 April 1998.
6. Tozaki Y, Uematsu Y, Tokaji K (2007) Effect of processing parameters on static strength of dissimilar friction stir spot welds between different aluminium alloys. *Fatigue Fracture Eng Mater Struct* 30:143–148
7. Zulu MC, Mashini PM (2018) Process optimization of rotary friction welding of Ti-6Al-4V alloy rods. *IOP Conf Ser Mater Sci Eng* 430:012012
8. Ramesh AP, Subramaniyan M, Eswaran P (2019) Review on friction welding of similar/dissimilar metals. *J Phys Conf Ser* 1362:012032
9. Guo W, You G, Yuan G, Zhang X (2017) Microstructure and mechanical properties of dissimilar inertia friction welding of 7A04 aluminum alloy to AZ31 magnesium alloy *J Alloys*
10. Fratini L, Barcellona A, Buffa G, Palmeri D (2007) *Proc. 1 Mech. Eng.* 221 Part B. *J. Engineering Manufacturing*.
11. Sun Y, Voyiadjis GZ, Hu W, Shen F, Meng Q (2017) Fatigue and fretting fatigue life prediction of double-lap bolted joints using continuum damage mechanics-based approach. *Int J Damage Mech* 6:162–188
12. Shen Z, Ding Y, Chen J, Gerlich AP (2016) Comparison of fatigue behavior in Mg/Mg similar and Mg/steel dissimilar refill friction stir spot welds. *Int J Fatigue* 92:78–86
13. Plaine AH, Suhuddin UFH, Alcântara NG, dos Santos JF (2016) Fatigue behavior of friction spot welds in lap shear specimens of AA5754 and Ti6Al4V alloys. *Int J Fatigue* 91:149–157
14. AnantSagar DB, Pardhu Y, Rao MSK, Narasaiah N (2022) Strain hardening behavior of friction welded beta titanium alloy Titan 1023 used for aeronautical applications. *Mater. Today*.

15. Nasution AK, Nawangsari P, Junaedi A, Hermawan H (2019) Friction welding of AZ31-SS316L for partially-degradable orthopaedic pins. *IOP Conf Ser Mater Sci Eng* 532:012014
16. Chekroun N, Mimouni O, Badji R, Gassaa R, Hadji M (2016) Numerical simulation of temperature distribution and material flow during friction stir welding 2017A aluminum alloys. *MATEC Web of Conferences* 80:12002
17. Mir FA, Khan NZ, Parvez S (2021) Recent advances and development in joining ceramics to metals. *Mater Today Proc* 46:6570–6575
18. Uday MB, Ahmad-Fauzi MN, Noor AM, Rajoo S (2015) An insight into microstructural evolution during plastic deformation in AA6061 alloy after friction welding with alumina-YSZ composite. *Mech Mater* 91:50–63
19. Rombaut P, De Waele W, Faes K (2011) Friction welding of steel to ceramic. In *Sustainable Construction and Design 2011 (SCAD)*; Ghent University, Laboratory Soete: Ghent, Belgium, 2011; Volume 2011.
20. Li P, Li J, Dong H, Ji C (2017) Metallurgical and mechanical properties of continuous drive friction welded copper/alumina dissimilar joints. *Mater Des* 127:311–319
21. Eslami S, Farahani BV, Tavares PJ, Moreira PMGP (2018) Fatigue behaviour evaluation of dissimilar polymer joints: friction stir welded, single and double-rivets. *Int J Fatigue* 113:351–358
22. Cederqvist L (2000) Properties of friction stir welded aluminum lap joints. In *Proceedings of the 2nd FSW Symposium 2000*, Gothenburg, Sweden, 27–29 June 2000.
23. Sonne MR, Tutum CC, Hattel JH, Simar A, De Meester B (2013) The effect of hardening laws and thermal softening on modeling residual stresses in FSW of aluminum alloy 2024–T3. *J Mater Process Technol* 213:477–486
24. Cao X, Jahazi M (2011) Effect of tool rotational speed and probe length on lap joint quality of a friction stir welded magnesium alloy. *Mater Des* 32:1–11
25. Nandan R, DebRoy T, Bhadeshia H (2008) Recent advances in friction-stir welding-process, weldment structure and properties. *Prog Mater Sci* 53:980–1023
26. PrasannaNagasai B, Malarvizhi S, Balasubramanian V (2022) Mechanical properties and microstructural characteristics of AA5356 aluminum alloy cylindrical components made by wire arc additive manufacturing process. *Mater Per Cha* 11(1):1–26
27. Raja S, SachinAdithyaa A, Sai Yaswanth V, Saranya R, Sabarivasan U (2020) Establishing an empirical relationship to predict strength of dissimilar friction welded steel joints. *Paideuma J* 13(7):68–82
28. Paulo Davim. (2021) *Welding technology. Materials forming, machining and tribology*. Springer Nature Switzerland AG 2021. ISBN 978–3–030–63985–3.
29. Kapil Gupta J, Paulo Davim J, Paulo Davim. (2021) *Advanced welding and deforming*. April 17, 2021. Elsevier 2021, ISBN: 9780128220498.
30. Pawan Kumar Rakesh, J Paulo Davim. *Joining processes for dissimilar and advanced materials*, Elsevier, 2021, ISBN: 9780323853996
31. Vairamani G, Senthilkumar T, Malarvizhi S, Balasubramanian V (2013) Predicting tensile strength and interface hardness of friction welded dissimilar joints of austenitic stainless steel and aluminium alloy by empirical relationships. *The Ind. Ins. Wel.* 46(2):67–75
32. Kumar Rajak D, Pagar DD, Menezes PL, Eyvazian A (2020) Friction-based welding processes: Friction welding and friction stir welding. *J Adhes Sci Technol* 34:2613–2637
33. Emami S, Sadeghi-Kanani S, Saeid T et al (2020) Dissimilar friction stir welding of AISI 430 ferritic and AISI 304L austenitic stainless steels. *Arch Civil MechEng* 20:1–16
34. Shanjeevi C, Arputhabalan J, Pavithran E, Raju B (2019) Prediction of optimized friction welding parameter for joining of dissimilar material using friction welding. *Mater. Today Proc.* 2019, 16, 838–842. *Proc.* 2022, 57, 687–692.
35. Paventhan R, Lakshminarayanan PR, Balasubramanian V (2012) Optimization of friction welding process parameters for joining carbon steel and stainless steel. *J Iron Steel Res Int.* 19:66–71. *Compd.* 2017, 695, 3267–3277
36. Biallas G, Braun R, Dalle Donne C, Staniek G, Kaysser WA (1999) Mechanical properties and corrosion behavior of friction stir welded 2024-T3. *Proceedings of the 1st International Friction Stir Welding Symposium*, Thousand Oaks, California.
37. Mahoney MW, Rhodes CG, Flintoff JG, Spurling RA, Bingel WH (1998) Properties of friction stir welded 7075–T651 aluminum. *Metall and Mater Trans A* 29A:1955–1964
38. Vairamani G, Senthil kumar T, Malarvizhi S, Balasubramanian V (2013) Developing empirical relationships to predict tensile strength and interface hardness of friction welded medium carbon steel - austenitic stainless steel joints, *IWS J.* 21–27.
39. Vairamani G, Senthilkumar T, Malarvizhi S, Balasubramanian V (2013) Application of response surface methodology to maximize tensile strength and minimize interface hardness of friction welded dissimilar joints of austenitic stainless steel and copper alloy. *Tran Nonferrous Met Soc Chi* 23(8):2250–2259
40. Nagasai BP, Malarvizhi S, Balasubramanian V (2021) Mechanical properties of wire arc additive manufactured carbon steel cylindrical component made by gas metal arc welding process. *J Mech Beha Mat* 30:188–198
41. Christner B, McCoury J, Higgins S (2003) Development and testing of friction stir welding (FSW) as a joining method for primary aircraft structure. In *Proceedings of the 4th International Friction Stir Welding Symposium 2003*, Park City, UT, USA, 14–16 May 2003.
42. Thomas WM (1998) Friction stir welding and related friction process characteristics. *Proceedings of the 7th International Conference on Joints in Aluminum (INALCO'98)*, Cambridge, UK, April 1998.
43. Akinlabi ET (2012) Effect of shoulder size on weld properties of dissimilar metal friction stir welds [J]. *J Mater Eng Perform* 21(7):1514–1519
44. Thomas WM, Nicholas ED (1997) Friction stir welding for the transportation industry. *Mater Des* 18(4/6):269–273
45. Thomas WM, Nicholas ED, Needham JC, Murch P, Temple-Smith, P, Dawes CJ (1991) Friction-stir butt welding. GB Patent Application No. 9125978.8, International Patent Application PCT/GB92/02203, 6 December 1991.
46. Thomas WM, Nicholas ED, Watts ER, Staines DG (2002) Friction based welding technology for aluminum, *Proceedings of the 8th International Conference on Aluminum Alloys*, Cambridge, UK, 2–5 July 2002.
47. Midling OT, Oosterkamp LD, Bersaas J (1998) Friction stir welding – process and applications, *Proceedings of 7th International Conference on Joints in Aluminum*, Cambridge, UK, 15–17 April 1998.
48. Sanderson A, Punshon CS, Russell JD (2000) Advanced welding processes for fusion reactor fabrication. *Fusion Eng Des* 49–50:77–87
49. Nandan R, DebRoy T, Bhadeshia H (2008) Recent advances in friction-stir welding-process, weldment structure and properties. *Prog Mater Sci* 53:980–1023
50. Riahi M, Nazari H (2011) Analysis of transient temperature and residual thermal stresses in friction stir welding of aluminum alloy 6061–T6 via numerical simulation. *Int J Adv Manuf Technol* 55:143–152
51. Veljić DM, Rakin MP, Perović MM, Međo BI, Radaković ZJ, Todorović PM, Pavišić MN (2013) Heat generation during plunge stage in friction stir welding. *Therm Sci* 17:489–496
52. Al-Badour F, Merah N, Shuaib A, Bazoune A (2013) Coupled Eulerian Lagrangian finite element modeling of friction stir welding processes. *J Mater Process Technol* 213:1433–1439

53. Bussetta P, Dialami N, Boman R, Chiumenti M, Agelet de Sarcibar C, Cervera M, Ponthot JP (2014) Comparison of a fluid and a solid approach for the numerical simulation of friction stir welding with a non-cylindrical pin. *Steel Res Int* 85:968–979
54. Aziz SB, Dewan MW, Huggett DJ, Wahab MA, Okeil AM, Liao TW (2016) Impact of friction stir welding (FSW) process parameters on thermal modeling and heat generation of aluminum alloy joints. *Acta Metall Sin* 29:869–883
55. Sun T, Roy M, Strong D, Withers PJ, Prangnell PB (2017) Comparison of residual stress distributions in conventional and stationary shoulder high-strength aluminum alloy friction stir welds. *J Mater Process Technol* 242:92–100
56. Garg A, Bhattacharya A (2017) On lap shear strength of friction stir spot welded AA6061 alloy. *J Manuf Process* 26:203–215
57. Jain R, Pal SK, Singh SB (2017) Finite element simulation of temperature and strain distribution during friction stir welding of AA2024 aluminum alloy. *J Inst Eng Ser C* 98:37–43
58. Maisonnète D, Bardel D, Robin V, Nelias D, Suery M (2017) Mechanical behaviour at high temperature as induced during welding of a 6xxx series aluminium alloy. *Int J Press Vessel Pip* 149:55–65
59. Palanivel R, Dinaharan I, Laubscher RF, Paulo Davim J (2016) Influence of boron nitride nanoparticles on microstructure and wear behavior of AA6082/TiB₂ hybrid aluminum composites synthesized by friction stir processing. *Materials and Design* 106:195–204

Publisher's Note Springer Nature remains neutral with regard to jurisdictional claims in published maps and institutional affiliations.

Springer Nature or its licensor (e.g. a society or other partner) holds exclusive rights to this article under a publishing agreement with the author(s) or other rightsholder(s); author self-archiving of the accepted manuscript version of this article is solely governed by the terms of such publishing agreement and applicable law.